Supplementary Information for

Spectroscopic evidence of flat bands in breathing kagome semiconductor Nb_3I_8

Sabin Regmi,[1] Tharindu Warnakulasooriya Fernando,[2] Yuzhou Zhao,[2] Anup Pradhan Sakhya,[1] Gyanendra Dhakal,[1] Iftakhar Bin Elius,[1] Hector Vazquez,[1] Jonathan D Denlinger,[3] Jihui Yang,[4] Jiun-Haw Chu,[2] Xiaodong Xu,[2] Ting Cao,[4] and Madhab Neupane[1]

[1]*Department of Physics, University of Central Florida, Orlando, Florida 32816, USA*
[2]*Department of Physics, University of Washington, Seattle, Washington 98195, USA*
[3]*Lawrence Berkeley National Laboratory, Berkeley, California 94720, USA*
[4]*Department of Materials Science and Engineering, University of Washington, Seattle, Washington 98195, USA*

Supplementary Note 1. Crystal structure and sample characterization

Nb_3I_8 has a layered crystal structure (rhombohedral space group no. 166) with intralayer covalent bonding and interlayer van der Waal bonding along the crystallographic c-axis. A side view of the bulk crystal structure is shown in Supplementary Fig. 1a where a unit cell consists of sixtuple layers. Nb atoms are sandwiched in between two sheets of I atoms with I1, I3 atoms forming the top sheet and I2, I4 forming the bottom sheet. Top view of the crystal structure is presented in Supplementary Fig. 1b. Nb atoms form a breathing kagome lattice [see Supplementary Fig. 1c]. An schematic of breathing kagome lattice is shown in Supplementary Fig. 1e, where the alternating triangles are of unequal size unlike in conventional kagome lattice in which all the triangles are of equal size [Supplementary Fig. 1(d)].

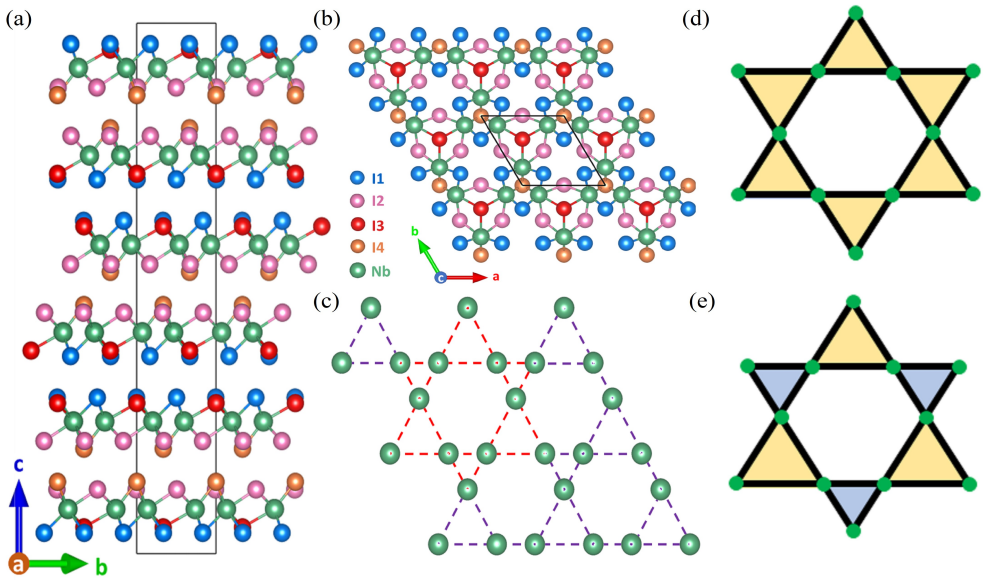

Supplementary Fig. 1: **Crystal structure and kagome geometry in Nb_3I_8. a** Side view and **b** top view of the crystal structure. **c** Breathing kagome plane formed by Nb atoms. **d-e** Schematic of conventional kagome and breathing kagome lattices, respectively.

As mentioned in the method section of the main text, high-quality single crystals of Nb_3I_8 used in this study were grown by employing chemical vapor transport method with Iodine used as a transport agent. The crystal structure was examined using X-ray diffraction (XRD). XRD on a Nb_3I_8 crystal grown in the same batch as the ARPES measurements is presented in Supplementary Fig. 2a. Sharp (000l) peaks are observed indicating that the crystal surface is oriented in the ab-plane. The compositional homogeneity of the crystals were verified using scanning electron microscopy (SEM) and energy dispersive X-ray spectroscopy analysis (EDS) performed on Nb_3I_8 flakes exfoliated on a SiO_2/Si substrate [see Supplementary Fig. 2b]. The quantitative elemental analysis shows a Nb : I ratio of 8.24:22.31 = 2.96:8 [see table 1].

Supplementary Table 1: EDS analysis of Nb_3I_8.

Element	Atomic Number	Series	Wt%	Wt% Sigma	Atomic%
Silicon	14	K Series	29.86	1.26	54.20
Iodine	53	L Series	55.53	1.64	22.31
Oxygen	8	K Series	4.78	0.8	15.24
Niobium	41	L Series	15.02	0.56	8.24

Supplementary Note 2. First-principle calculations

First-principles calculations were performed, for bulk stable state (Antiferromagnetic) and monolayer stable state (FM), utilizing the density functional theory approach [1, 2] as implemented in the QUANTUM ESPRESSO package [3] by using norm-conserving scalar relativistic ONCVPSP (Optimized Norm-Conserving Vanderbilt Pseudopotential) [4, 5] and Perdew-Burke-Ernzerhof-type exchange-correlational functional [6] and with van der Waals correction included in the D2 formalism [7]. A conventional unit cell with six layers with $a = 7.600$ Å and $c = 41.715$ Å [8] was used for the bulk calculations, and a single Nb_3I_8 layer with $c = 52.500$ Å was considered for monolayer

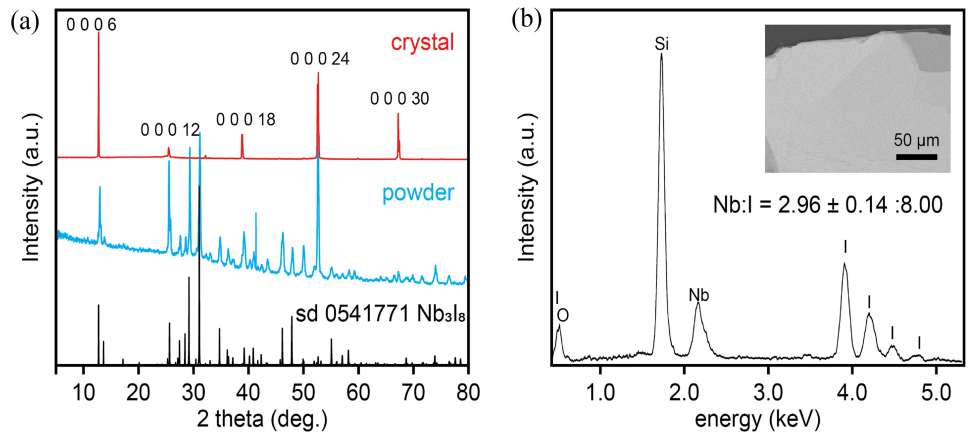

Supplementary Fig. 2: **Sample characterization.** **a** X-ray Diffraction (XRD) on powdered (cyan) and single crystal (red) Nb_3I_8. **b** Energy-dispersive X-ray spectroscopy (EDS) of Nb_3I_8 flakes exfoliated on a SiO_2/Si substrate.

calculations. Interlayer AFM was considered with each consecutive layers in six layers having alternate spins. Hubbard potential $U = 2$ eV on Nb d orbitals was used to account for the on-site interaction [9]. Convergence tests were run to justify a kinetic energy cutoff, $ecutwfc = 85$ Ry, and an 8 x 8 x 1 Monkhorst-Pack k-point grid. We used a convergence threshold (for self-consistency) of 1×10^{-8} Ry .

In Supplementary Fig. **3**, DFT calculations for bulk as well as monolayer Nb_3I_8 are presented. For comparison with experimental data, we set the mid-band gap to be the zero-energy level. The overall band structures of bulk and monolayer look similar. Direct Kohn-Sham band gap at the K point for bulk is ~ 520 meV and that of monolayer is ~ 490 meV indicating semiconducting nature of Nb_3I_8 in both three- and two-dimensions. We calculated the mirror operator eigenvalues of -1, 1, 1, 1, -1, 1, and -1 for the bands c3, c2, c1, v1, v2, v3, v4, and v5 bands (see Supplementary Fig. **4** for monolayer Kohn-Sham bands), respectively. With the inclusion of spin-orbit coupling (SOC), the band degeneracy of these bands at the Γ point is broken, indicative of potential topological character. For c1 and v1, no band inversion occurs, therefore these bands are non-topological. For bands c2, c3, v2, v3, v4, and v5, since any of these SOC-gapped bands cannot be completely isolated in energy by shifting the Fermi level (unlike band v1), quantized non-zero Chern numbers do not exist in this band structure by rigidly shifting the Fermi level alone.

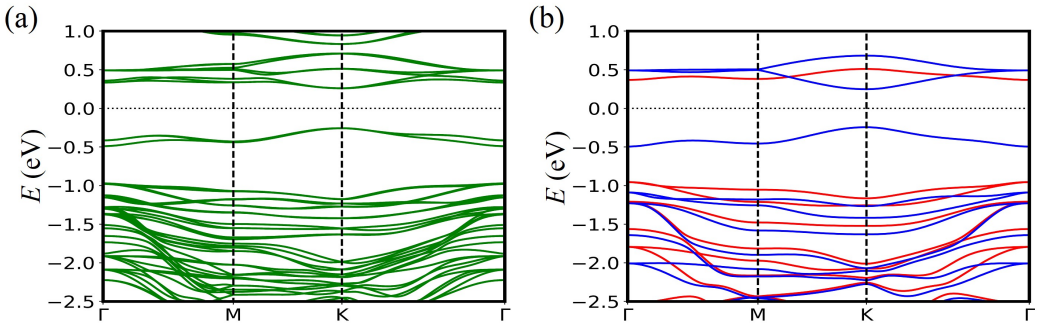

Supplementary Fig. 3: **Bulk and monolayer band calculations.** **a** DFT band structure calculation for bulk Nb_3I_8. For bulk, majority- and minority-spin bands are degenerate. **b** DFT band structure calculation for monolayer Nb_3I_8. Blue and red denote majority- and minority-spin bands, respectively.

In Supplementary Fig. **5**, we present the calculations for bulk Nb_3I_8 at different k_z planes (0 and π). Note that these calculations have been implemented in VASP [10]. The overall band structure remains similar to the one obtained by implementing in QUANTUM ESPRESSO. Also, the band structure within the bands of interest (flat and weakly dispersing bands that lie well within 1.5 eV) does not have significant difference for $k_z = 0$ and $k_z = \pi$ planes.

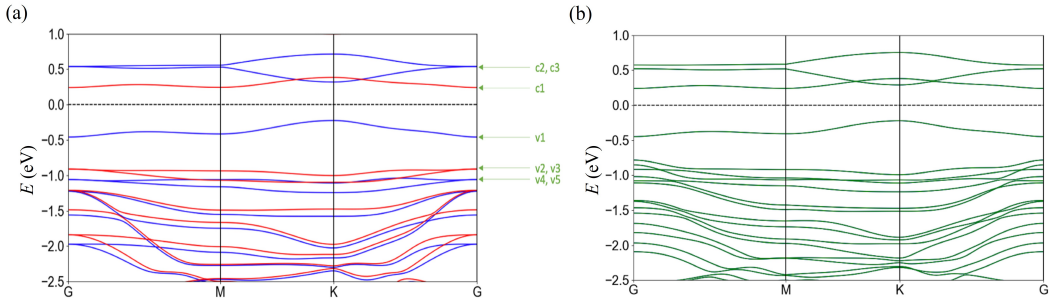

Supplementary Fig. 4: **Kohn-Sham bands of monolayer Nb_3I_8.** **a** Calculated Kohn-Sham bands without considering SOC. **b** Kohn-Sham bands with SOC included.

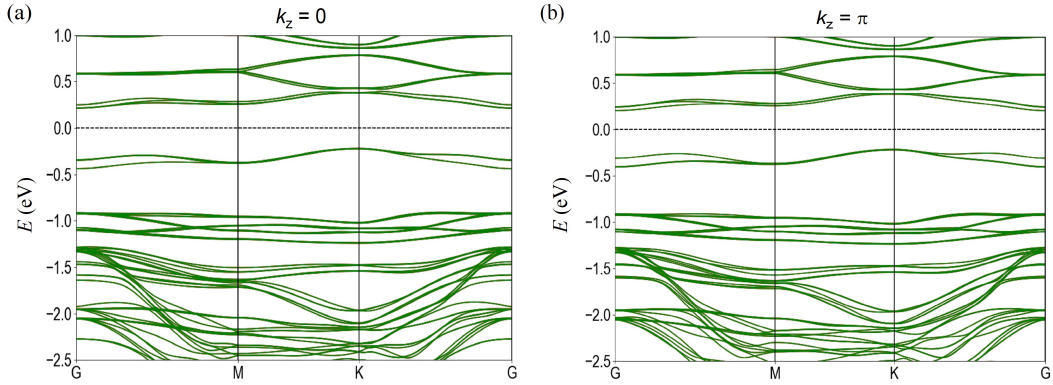

Supplementary Fig. 5: **Bulk bands calculated for different k_z planes.** DFT band calculations for bulk Nb_3I_8 for **a** $k_z = 0$ and **b** $k_z = \pi$ planes. The calculations are performed using VASP software [10].

Supplementary Note 3. Experimental details

Experimental measurements using the angle-resolved photoemission spectroscopy (ARPES) technique were carried out at the Advanced Light Source Beamline 4.0.3 equipped with Scienta R8000 hemispherical electron analyzer in the Berkeley National Laboratory. Single crystals of Nb_3I_8 were cleaved in-situ in ultra-high vacuum conditions to achieve clean and fresh surface. Measurements were done at a temperature of 260 K in order to dodge the charging effects. For the whole measurement period, the sample surface was stable and showed no sign of degradation. Energy and angular resolutions were set to be better than 20 meV and 0.2°, respectively. Photon beam with monoenergy in the range 30-124 eV was used with linear horizontal (LH) and linear vertical polarization (LV).

An experimental geometry for the ARPES measurements is shown in Supplementary Fig. **6**. At normal emission, the beam is incident at a 25° grazing angle to the sample, i.e. the angle between the x-rays and Scienta lens axis is fixed at 65°. The Scienta electron analyzer is mounted with a

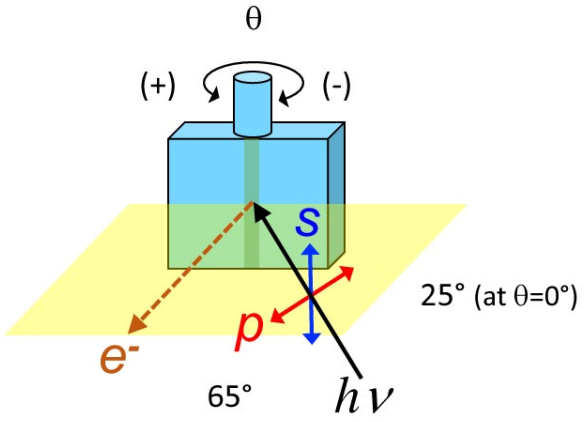

Supplementary Fig. 6: Experimental geometry used in the ARPES measurements.

vertical slit and a polar map rotates the sample about a vertical axis. LH (LV) polarization oscillates the electrons in the undulator in the horizontal (vertical) plane and so the x-ray polarization vector is in the horizontal (vertical) plane of the incident x-ray propagation direction. When the sample tilt angle is zero, then LV polarization gives purely s-polarization (polarization vector in the plane of the sample surface). LH polarization has both s- and p-polarization components, which depend on the polar angle (θ) as: $e_p = cos(\theta + 25°)$ and $e_s = sin(\theta + 25°)$. For our polarization dependent cuts, the value of θ is -4°.

Supplementary Note 4. Photon energy dependent dispersion maps

In order to show the two-dimensional (2D) nature of the flat bands, we show the photon energy dependent dispersion maps along the $\overline{\mathrm{M}} - \overline{\Gamma} - \overline{\mathrm{M}}$ direction in Supplementary Fig. 7. Similar to what was observed with the photon energy variation in the main text, the flat bands do not change their dispersion with changing photon energy (only the photoemission intensity is changing). This confirms that these bands are indeed of 2D nature. On the other hand, the dispersing bands seem to be dependent on photon energy showing their three-dimensional bulk origination.

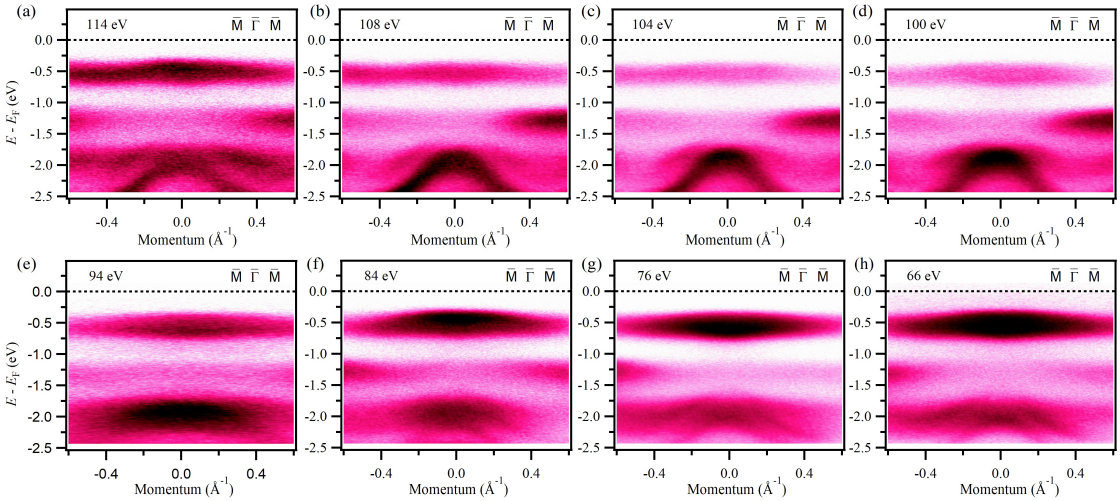

Supplementary Fig. 7: **Photon energy-dependent dispersion maps. a-h** Dispersion maps along the $\overline{\mathrm{M}} - \overline{\Gamma} - \overline{\mathrm{M}}$ direction for different value of photon mono-energy. The energy values are noted on each plots.

Supplementary Note 5. Orbital resolved band structure calculations

Supplementary Fig. 8a shows the total contribution from Noibium d in the electronic structure along $\mathrm{M} - \Gamma - \mathrm{M}$. We can see strong contribution of Nb d to the bands A - C. Subsequent plots

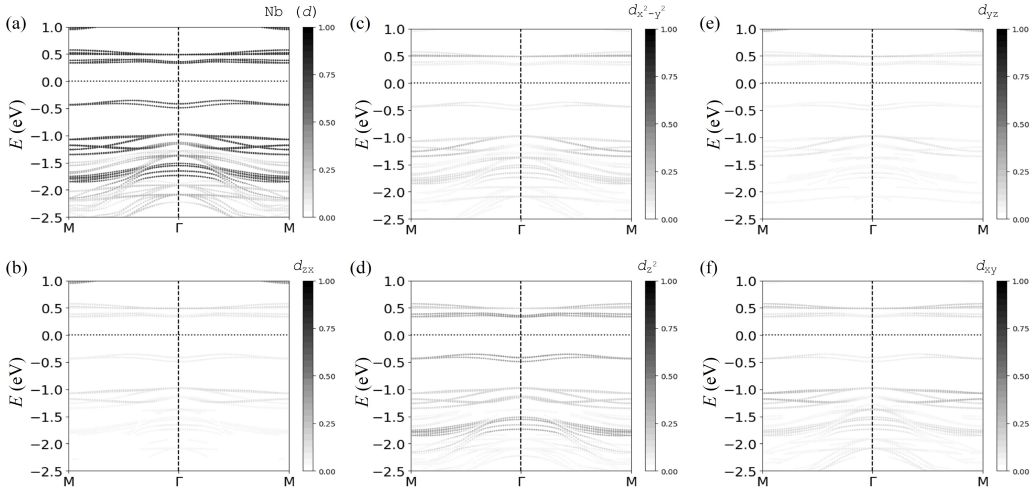

Supplementary Fig. 8: **Contribution from individual Nb d orbitals. a** Dispersion map along the $\mathrm{M} - \Gamma - \mathrm{M}$ direction with total contribution from Nb d orbitals. **b-f** Band structure showing individual contributions from d_{zx}, $d_{x^2-y^2}$, d_{z^2}, d_{yz}, and d_{xy} orbitals, respectively.

in Supplementary Figs. 8b-f present the individual contribution from d_{zx}, $d_{x^2-y^2}$, d_{z^2}, d_{yz}, and d_{xy} orbitals, respectively. It can be seen that the bands A and B have strong dominance from d_{z^2} orbitals. The bandset C, on the other hand, seem to have significant contribution coming from all orbitals with majority contribution coming from d_{xy} orbitals.

Supplementary Note 6. Energy distribution curves (EDCs)

In Supplementary Fig. 9, we present the EDCs (both raw and fits using voigt function) for the plots used in main text Figs. 3a and 4d. We can observe that the intensity of the flat and weakly dispersing bands coming from Nb breathing kagome plane depend upon the polarization of the incident photon beam. The bands around 500 meV (A and B), which have dominant d_{z^2} orbital character appear strong when the incident beam is LH polarized. On the other hand, the bands below 1.2 eV (bandset C) with major d_{xy} orbital contribution are enhanced when the incident photon beam is LV polarization.

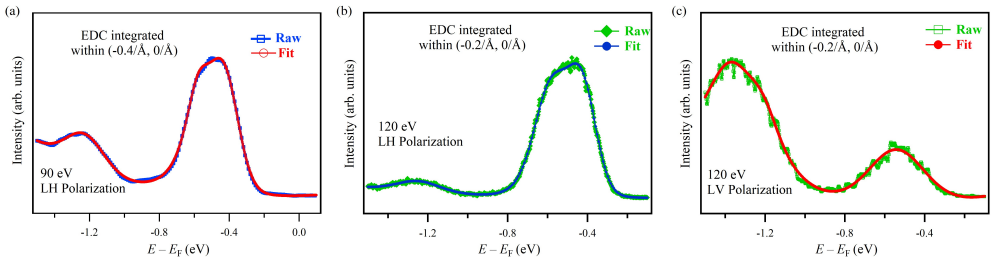

Supplementary Fig. 9: **Energy distribution curves and Voigt fits.** EDCs and respective fits using voigt function for **a** 90 eV linear horizontal polarized light, **b** 120 eV linear horizontal polarized light, and **c** 120 eV linear vertical polarized light.

Supplementary Note 7. Optical and atomic force microscopy images

In Supplementary Fig. 10, we present the images of the exfoliated Nb_3I_8 samples. Panel (a) shows the optical image of the crystal that is exfoliated and the panels (b) and (c) show the optical image and atomic force microscopy images after exfoliation onto SiO_2/Si substrate. Our images reveal that the bulk Nb_3I_8 crystals can be exfoliated into thinner flakes, thereby indicating the potential utilization in two-dimensional heterostructure studies and applications.

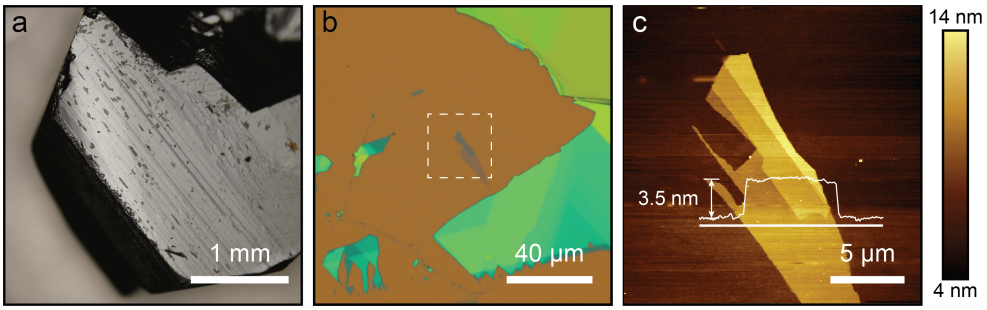

Supplementary Fig. 10: **Exfoliation of Nb_3I_8. a** Optical image of crystal before exfoliation. **b,c** Optical image and atomic force microscopy image of exfoliated Nb_3I_8 samples.

Supplementary References

[1] Hohenberg, P. & Kohn, W. Inhomogeneous Electron Gas. *Phys. Rev.* **136,** B864 (1964).

[2] Kohn, W. & Sham, L. J. Self-Consistent Equations Including Exchange and Correlation Effects. *Phys. Rev.* **140,** A1133 (1965).

[3] Giannozzi, P. et al. QUANTUM ESPRESSO: a modular and open-source software project for quantum simulations of materials. *J. Phys. Condens. Mater.* **21,** 395502 (2009).

[4] Hamann, D. R. Optimized norm-conserving Vanderbilt pseudopotentials. *Phys. Rev. B* **88,** 085117 (2013).

[5] Hamann, D. R. Erratum: Optimized norm-conserving Vanderbilt pseudopotentials [Phys. Rev. B 88, 085117 (2013)]. *Phys. Rev. B* **95,** 239906 (2017).

[6] J. P. Perdew, K. Burke, and M. Ernzerhof, Generalized Gradient Approximation Made Simple, Phys. Rev. Lett. **77**, 3865 (1996).

[7] Grimme, S. Semiempirical GGA-type density functional constructed with a long-range dispersion correction. *J. Comput. Chem.* **27,** 1787 (2006).

[8] Magonov, S. N. et al. Scanning tunneling and atomic force microscopy study of layered transition metal halides Nb_3X_8 (X = Cl, Br, I). *J. Am. Chem. Soc.* **115,** 2495 (1993).

[9] Jiang, J. et al. Exploration of new ferromagnetic, semiconducting and biocompatible Nb_3X_8 (X = Cl, Br or I) monolayers with considerable visible and infrared light absorption. *Nanoscale* **9,** 2992 (2017).
[10] Kresse, G. & Furthmüller, J. Efficient iterative schemes for ab initio total-energy calculations using a plane-wave basis set. *Phys. Rev. B* **54,** 11169 (1996).